arXiv:2206.04006v2 [cs.SD] 24 Nov 2022

Few-Shot Audio-Visual Learning of Environment Acoustics

Sagnik Majumder[1] **Changan Chen**[1,2*] **Ziad Al-Halah**[1*] **Kristen Grauman**[1,2]
[1]UT Austin [2]FAIR

Abstract

Room impulse response (RIR) functions capture how the surrounding physical environment transforms the sounds heard by a listener, with implications for various applications in AR, VR, and robotics. Whereas traditional methods to estimate RIRs assume dense geometry and/or sound measurements throughout the environment, we explore how to infer RIRs based on a sparse set of images and echoes observed in the space. Towards that goal, we introduce a transformer-based method that uses self-attention to build a rich acoustic context, then predicts RIRs of arbitrary query source-receiver locations through cross-attention. Additionally, we design a novel training objective that improves the match in the acoustic signature between the RIR predictions and the targets. In experiments using a state-of-the-art audio-visual simulator for 3D environments, we demonstrate that our method successfully generates arbitrary RIRs, outperforming state-of-the-art methods and—in a major departure from traditional methods—generalizing to novel environments in a few-shot manner. Project: `http://vision.cs.utexas.edu/projects/fs_rir`.

1 Introduction

Sound is central to our perceptual experience—people talk, doorbells ring, music plays, knives chop, dishwashers hum. A sound carries information not only about the *semantics* of its source, but also the *physical space* around it. For instance, compare listening to your favorite song in a big auditorium to hearing the same song in your cozy bedroom: the auditory experience changes drastically due to differences in the environment. On its way to our ears, sound undergoes various acoustic phenomena: direct sound, early reflections, and late reverberations. Consequently, we hear spatial sound shaped by the environment's geometry, the materials of constituent surfaces and objects, and the relative locations of the sound source and the listener. These factors together comprise the *room impulse response* (RIR)—the transfer function that maps an original sound to the sound that meets our ears or microphones [64].

Learning to model RIRs would have far-reaching implications for augmented reality (AR), virtual reality (VR), and robotics. In AR/VR, a truly immersive experience demands that the user hear sounds that are *acoustically matched* with the surrounding augmented/virtual space [66]. For example, imagine a situation in which users of an AR/VR app, who are at different locations, are speaking to each other through telepresence and moving about during the conversation. In mobile robotics, an agent cognizant of environment acoustics could better solve important embodied tasks, like localizing sounds, navigating to a target sound, or separating out a target sound(s) of interest. In any such application, one must be able to anticipate the environment effects for arbitrarily positioned sources observed from arbitrary receiver poses.

Traditional approaches to model room acoustics require extensive access to the physical environment. They either assume a full 3D mesh of the space is available in order to simulate sound propagation

*Equal contribution

36th Conference on Neural Information Processing Systems (NeurIPS 2022).

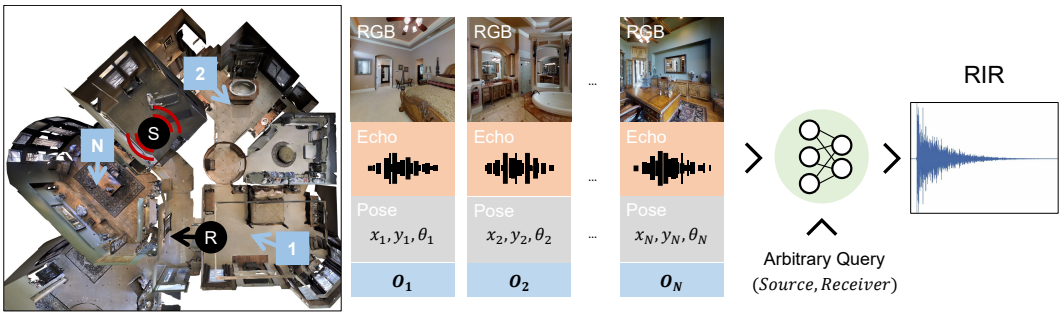


Figure 1: Given few-shot audio-visual observations from a 3D scene (blue boxes), we aim to learn an acoustic model for the entire environment such that we can generate a Room Impulse Response (RIR) for any arbitrary query of source (S) and receiver (R) locations in the scene—*without* observing images/echoes at those locations.

patterns [10, 42], or else require densely sampling sounds at many source-microphone position pairs all about the environment in order to measure the RIRs [25, 62]—both of which are expensive if not impractical. Recent work attempts to lighten these requirements by predicting (sometimes implicitly) the RIR from an image [59, 32, 22, 71, 68, 48, 9], but their output is specific to a single receiver position for which the photo exists, prohibiting generalization to other positions in the space.

Mindful of these limitations, we propose to infer RIRs in novel environments using only few-shot audio-visual observations. Motivated by how humans anticipate the overall structure of a 3D space by looking at a few parts of it, we hypothesize that imagery and echoes captured from a few different locations in a 3D scene can suggest its overall geometry and material composition, which in turn can facilitate interpolation of an RIR to arbitrary (unobserved) locations. See Figure 1.

To realize this idea, we propose a transformer-based model called FEW-SHOTRIR along with a novel training objective that facilitates high-quality prediction of RIRs by matching the energy decay between the predicted and the ground truth RIRs. FEW-SHOTRIR directly attends to the egocentric audio-visual observations to build an acoustic context of the environment. During training, our model learns the association between what is seen and heard in a variety of environments. Then, given a novel environment (e.g., a previously unseen multi-room home), the input is a sparse (few-shot) set of images together with the true RIRs at those image positions. In particular, each true RIR corresponds to positioning both the source and receiver where the image is captured, as obtained by emitting a short frequency sweep and recording the echoes. The output is an environment-specific function that can predict the RIR for arbitrary new source/receiver poses in that space—importantly, *without* traveling there or sampling any further images or echoes.

Our design has three key advantages: 1) the few-shot sparsity of the observations (on the order of tens, compared to the thousands that would be needed for dense visual or geometric coverage) means that RIR inference in a new space has low overhead; 2) the use of egocentric echoes means that the preliminary observations are simple to obtain, as opposed to repeatedly moving both a sound source (e.g., speaker) and the microphone independently to different relative positions; and 3) our novel differentiable training loss encourages predictions that capture the room acoustics, distinct from existing models that rely on non-differentiable RT60 losses [59, 53].

We evaluate FEW-SHOTRIR with realistic audio-visual simulations from SoundSpaces [10] comprising 83 real-world Matterport3D [7] environment scans. Our model successfully learns environment acoustics, outperforming the state-of-the-art models in addition to several baselines. We also demonstrate the impact on two downstream tasks that rely on the spatialization accuracy of RIRs: sound source localization and depth prediction. Our margin of improvement over a state-of-the-art model is as high as 23% on RIR prediction and 67% on downstream evaluation.

2 Related Work

Audio Spatialization and Impulse Response Generation. Convolving an RIR with a waveform yields the sound of that source in the context of the surrounding physical space and the receiver location [4, 5, 18, 57]. Since traditional methods for measuring RIRs [25, 62] or simulating them

with sound propagation models [3, 10, 42] are computationally expensive, recent approaches indirectly generate RIRs by first estimating acoustic parameters [53, 15, 19, 31, 36, 67]—such as the reverberation time (RT60), the time an RIR takes to decay by 60 dB, and the direct-to-reverberant ratio (DRR), the energy ratio of direct and reflected sound—or matching the distributions of such acoustic parameters in real-world RIRs [51]. Whereas Fast-RIR [53] assumes that the environment size and reverberation characteristics are given, our model relies on learning directly from low-level multi-modal sensory information, thus generalizing to novel environments.

Alternately, some methods use images to predict RIRs of the target environment [59, 32] by implicitly inferring scene geometry [54] and acoustic parameters [32], or directly synthesizing spatial audio [22, 71, 68, 48, 9]. Although such image-based methods have the flexibility to extract diverse acoustic cues, their predictions are agnostic to the exact source and receiver locations, making them unsuitable for tasks where this mapping is important (e.g., sound source localization, audio goal navigation, or fine-grained acoustic matching).

Audio field coding approaches [49, 39, 50, 6] are able to model exact source and receiver locations, but to improve efficiency they rely on handcrafting features rather than learning them, which adversely impacts generation fidelity [35]. The recently proposed Neural Acoustic Fields (NAF) [35] tackles this by learning an implicit representation [41, 60] of the RIRs and additionally conditioning on geometrically-grounded learned embeddings. While NAF can generalize to unseen source-receiver pairs from the same environment, it requires training *one model per environment*. Consequently, NAF is unable to generalize to novel environments, and both its training time and model storage cost scale with the number of environments. On the contrary, given a few egocentric audio-visual observations from a novel environment, our model learns an implicit acoustic representation of the scene and predicts high-quality RIRs for arbitrary source-receiver pairs.

Audio-Visual Learning. Advances in audio-visual learning benefit many tasks, like audio-visual source separation and speech enhancement [1, 2, 12, 16, 26, 40, 44, 56, 69, 70, 37, 38], object/speaker localization [27, 29], and audio-visual navigation [10, 11, 8, 20, 14, 14]. Using echo responses along with vision to learn a better spatial representation [21], infer depth [13], or predict the floorplan [47] of a 3D environment has also been explored. In contrast, our model leverages the synergy of egocentric vision and echo responses to infer environment acoustics for predicting RIRs. Results show that both the visual and audio modalities play a vital role in our model training.

3 Few-Shot Learning of Environment Acoustics

We propose a novel task: few-shot audio-visual learning of environment acoustics. The objective is to predict RIRs on the basis of egocentric audio-visual observations captured in a 3D environment. In particular, for a few randomly drawn locations in the 3D scene, we are given egocentric RGB, depth images, and the echoes heard at those positions (from which the corresponding RIR can be computed, detailed below). Using those samples, we model the scene's acoustic space, in order to predict RIRs for arbitrary pairings of sound source location and receiver pose (i.e., microphone location and orientation).

Task Definition. Specifically, let $\mathcal{O} = \{O_i\}^N$ be a set of N observations ($N \leq 20$ in our experiments) randomly sampled from a 3D environment, such that $O_i = (V_i, A_i, P_i)$ where V_i is the egocentric RGB-D view from a 90° field of view (FoV), A_i is the RIR of the binaural echo response from a pose $P_i = (x_i, y_i, \theta_i)$ at location (x_i, y_i) and orientation θ_i. Given a query for an arbitrary source and receiver pair, $Q = (s_j, r_k)$, where $s_j = (x_j, y_j)$ is the omnidirectional sound source location and $r_k = (x_k, y_k, \theta_k)$ is the receiver microphone pose, which includes both its location and orientation, the goal is to predict the binaural RIR $\mathcal{R}^Q$ for the query Q. Thus, our goal is to learn a function f to predict the RIR for an arbitrary query Q given the egocentric audio-visual context $\{O_i\}^N$, such that $\mathcal{R}^Q = f(Q; \{O_i\}^N)$. Note that the query contains neither images nor echoes.

This task requires learning from both visual and audio cues. While the visual signal conveys information about the local scene geometry and the material composition of visible surfaces and objects, the audio signal, in the form of echo responses, is more long-range in nature and additionally carries cues about acoustic properties, the global geometric structure, and material distribution in the environment—beyond what's visible in the image. Our hypothesis is that sampling and aggregating

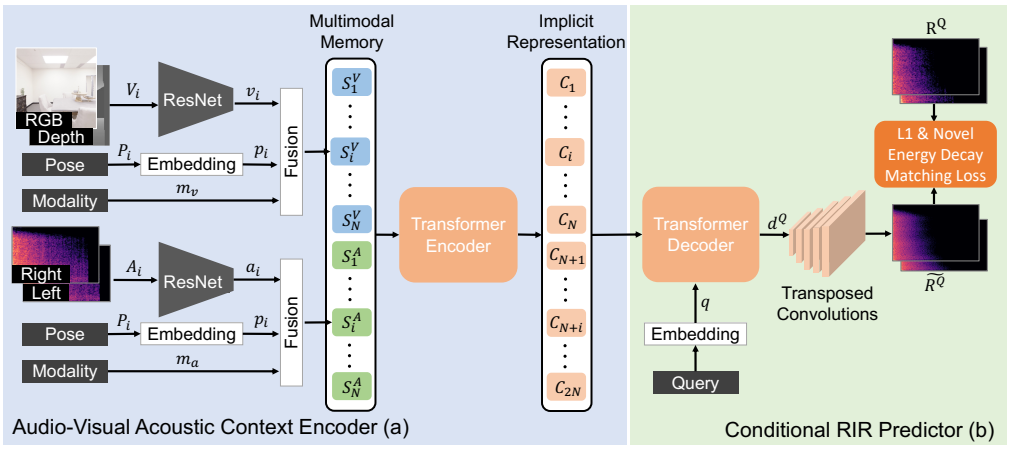


Figure 2: Our model predicts room impulse responses (RIR) for arbitrary source-receiver pairs in a 3D environment, including novel scenes, by building its implicit acoustic representation in the few-shot context of egocentric audio-visual observations. We train our model with a novel energy decay matching loss that helps capture desirable acoustic properties in its predictions.

these two complementary signals from a sparse set of locations in a 3D scene can facilitate inference of the full acoustic manifold and, consequently, enable high-quality prediction of arbitrary RIRs.

4 Approach

We introduce a novel approach called FEW-SHOTRIR for arbitrary RIR prediction in a 3D environment based on few-shot context of egocentric audio-visual observations. Our model has two main components (see Fig 2): 1) an audio-visual (AV) context encoder, and 2) a conditional RIR predictor. The AV context encoder builds an implicit model of the environment's acoustic properties by extracting multimodal cues from the input AV context (Sec.4.1). The RIR predictor uses this implicit representation of the scene and, conditioned on a query for an arbitrary source and receiver pair, it predicts the respective RIR (Sec.4.2).

Our model is trained end-to-end to reduce the error in the predicted RIR compared to the ground-truth using a novel training objective (Sec.4.3). Our objective not only encourages our model predictions to match the target RIRs at the spectrogram level, but also ensures that the predictions and the targets are similar with respect to important high-level acoustic parameters, thereby improving prediction quality. Next, we describe these two model components and the proposed training objective in detail.

4.1 Audio-Visual Context Encoder

Our AV context encoder (Fig. 2a) extracts features from the observations $\{O_i\}$. This context is sampled from the unmapped environment via an agent (a person or robot) traversing the scene and taking a small set of AV snapshots at random locations. Our model starts by embedding each observation $O_i = (V_i, A_i, P_i)$ using visual, acoustic, and pose networks. This is followed by a multi-layer transformer encoder [65] to learn an implicit representation of the scene's acoustic properties.

Visual-Embedding. We encode the visual component V_i by first normalizing its RGB and depth images such that all image pixels lie in the range $[0, 1]$. We then concatenate the images along the channel dimension and encode them with a network f^V (a ResNet-18 [24]) into visual features v_i.

Acoustic-Embedding. To measure the RIRs for the echo inputs, we use the standard sine-sweeping technique [17]. We first generate a "chirp" in the form of a sinusoidal sweep signal from 20Hz-20kHz (the human audible range) at the sound source, capture the resulting spatial sound with a microphone that has a (nearly) flat frequency response, and then retrieve the RIR at the receiver by convolving the spatial sound with the inverse of the sweep signal. We then use the short-time Fourier transform

(STFT) to represent all RIRs as magnitude spectrograms [59, 35] of size $2 \times F \times T$, where F is the number of frequency bins, T is the number of overlapping time windows, and each spectrogram has 2 channels. Finally, having converted the observed binaural echoes to an RIR A_i, we compute its log magnitude spectrogram and encode it with a network f^A (a ResNet-18 [24]) into audio features a_i.

Pose-Embedding. To embed the camera pose P_i into feature p_i, we first normalize all poses in $\{O_i\}$ to be relative to the first pose in the context P_0 and then represent each P_i with a sinusoidal positional encoding [65].

Modality-Embedding. To enable our model to distinguish between the visual and audio modalities in the context, we introduce a modality token $m_i \in \{m_V, m_A\}$ such that the visual m_V and acoustic m_A modality embeddings are learned during training. While the visual modality (RGB-D images) reveals the local geometric and semantic structure of the environment, the acoustic modality (the echoes) carry more global acoustic information about regions of environments that are both within and out of the field of view. Our modality-based embedding allows our model to attend within and across modalities to capture both modality-specific and complementary environmental cues for a comprehensive modeling of the acoustic properties of the scene.

Context Encoder. For each visual observation in $\{O_i\}$ we concatenate its embedding v_i with its pose p_i and modality m_V and project this representation with a single linear layer to get visual input S_i^V. Similarly, we concatenate a_i, p_i, and m_A and project it with another linear layer to get the acoustic input S_i^A. This creates a multimodal memory of size $2N$, such that $S = \{S_0^V, \ldots, S_N^V, S_0^A, \ldots S_N^A\}$. Next, our context encoder attends to the embeddings in S with self-attention to capture the short- and long-range correlations within and across modalities and through multiple layers to learn the implicit representation $C = \{C_1, \ldots, C_{2N}\}$ that models the acoustic properties of the 3D scene. This representation is then fed to the next module that generates the RIR for an arbitrary source-receiver query, as we describe next.

4.2 Conditional RIR Predictor

Given an arbitrary source-receiver query $Q = \{s_j, r_k\}$, we first normalize the poses of s_j and r_k relative to P_0 and encode each with a sinusoidal positional encoding as we did in Sec.4.1 to generate the pose encodings p_j^s and p_k^r, respectively. Then, we concatenate and project $[p_j^s, p_k^r]$ using a single linear layer to get the query encoding q. Next, our RIR predictor, conditioned on q, performs cross-attention on the learned implicit representation C using a transformer decoder [65], and generates an encoding d^Q that is representative of the target RIR for query Q (i.e., R^Q). Again, we stress that the query consists of only poses—no images or echoes.

We upsample d^Q with transpose convolutions using a multi-layer network U to predict the magnitude spectrogram in the log space for the RIR. Finally, we transform this log magnitude spectrogram back to the linear space to obtain our model's RIR prediction $\tilde{R}^Q$ for a query Q.

4.3 Model Training

Our model is optimized to predict the target RIR R^Q for a given query Q during training in a supervised manner using a loss L that captures both the prediction accuracy of the spectrogram as well as high-level acoustic properties of the predicted $\tilde{R}^Q$ compared to the ground truth R^Q. Our loss L contains two terms: 1) an L_1 reconstruction loss [59, 35] on the magnitude spectrogram of the RIR, and 2) a novel energy decay matching loss L_D.

For a target binaural spectrogram R^Q with F frequency levels and T temporal windows, the L_1 loss tries to reduce the average prediction error in the time-frequency domain:

$$L_1 = \frac{1}{2 \times F \times T} \sum_{i=1}^{2 \times F \times T} ||\tilde{R}_i^Q - R_i^Q||_1.$$

On the other hand, the L_D loss tries to capture the reverberation quality of the RIR by matching the temporal decay in energy of the predicted RIR with the target. L_D allows our model to reduce errors in important reverberation parameters that depend on the energy decay of the RIR, like RT60,

which is the time taken by an impulse to decay by 60 dB, and DRR, which is the direct-to-reverberant energy ratio (cf. Table 1). Although past approaches [59, 53] have tried to minimize the RT60 error directly, incorporating an RT60 loss in a training objective is not viable due to the non-differentiable nature of the RT60 function. On the contrary, our proposed L_D is completely differentiable and can be combined with any other RIR training objective.

To compute L_D, we first (similar to [59]) obtain the energy decay curve of an RIR by summing its spectrogram along the frequency axis to retrieve a full-band amplitude envelope, and then use Schroeder's backward integration algorithm to compute the decay curve $D_{\mathcal{E}}$. However, unlike [59], which computes the RT60 value from the decay curve through a series of non-differentiable operations, our L_D directly measures the error in the energy decay curve between the prediction and the target, which not only makes it completely differentiable but also useful for capturing different energy based acoustic properties other than RT60, like DRR and early decay time (EDT) [52]. Towards that goal, we compute the absolute error in $D_{\mathcal{E}}$ between $\tilde{R}^Q$ and the target R^Q for those temporal positions at which the target energy decay $D_{\mathcal{E}}(R^Q)$ is non-zero. This lets our model ignore optimizing for the all-zero tails in shorter RIRs. L_D is defined as follows:

$$L_D = \frac{1}{2 \times T} \sum_{i=1}^{2 \times T} ||D_{\mathcal{E}}(\tilde{R}^Q)_i - D_{\mathcal{E}}(R^Q)_i||_1 \odot \mathbb{1}[D_{\mathcal{E}}(R^Q)_i \neq 0]$$

Our final training objective is $L = L_1 + \lambda L_D$, where λ is the weight for L_D. We train our model using Adam [30] with a learning rate of 10^{-4} and $\lambda = 10^{-2}$.

5 Experiments

Evaluation setup. We evaluate our task using a state-of-the-art perceptually realistic 3D audio-visual simulator. In particular, we use the AI-Habitat simulator [58] with the SoundSpaces [10] audio and the Matterport3D scenes [7]. While Matterport3D contains dense 3D meshes and image scans of real-world houses and other indoor spaces, SoundSpaces provides pre-computed RIRs to render spatial audio at a spatial resolution of 1 meter for Matterport3D. These RIRs capture all major real-world acoustic phenomena (see [10] for details). This framework enables us to evaluate our task on a large number of environments, to test on diverse scene types, to compare methods under same settings, and to report reproducible results. To our knowledge, there is no existing public dataset having both imagery and dense physically measured RIRs. Furthermore, due to the popularity of this framework (e.g., [21, 11, 14, 37, 47, 9]) we can test our model on important downstream tasks for RIR generation that are relevant to the larger community.

Dataset splits. We evaluate with 83 Matterport3D scenes, of which we treat 56 randomly sampled ones as *seen* and the remaining 27 as *unseen*. Unseen environments are only used for testing. For the seen environments, we hold out a subset of queries Q for testing and use the rest for training and validation. Our test set consists of 14 sets of 50 arbitrary queries for each environment, where our model uses the same randomly chosen observation set for all queries in a set. This results in a train-val split with 8,107,904 queries, and a test split with 39,900 queries for *seen* and 18,200 queries for *unseen*. Our testing strategy allows us to evaluate a model on two different aspects: 1) for a given observation set from an environment, how the RIR prediction quality varies as a function of the query, and 2) how well the model generalizes to environments previously unseen during training.

Observations. We render all RGB-D images for our model input at a resolution of 128×128 and sample binaural RIRs at a rate of 16 kHz. To generate the RIR spectrograms, we compute the STFT with a Hann window of 15.5 ms, hop length of 3.875 ms, and FFT size of 511. This results in two-channel spectrograms, where each channel has 256 frequency bins and 259 overlapping temporal windows. Unless otherwise specified, for both training and evaluation, we use egocentric observation sets of size $N = 20$ samples for our model.

Existing methods and baselines. We compare our approach to the following baselines and state-of-the-art methods (see Supp. for implementation and training details):

- **Nearest Neighbor:** a naive baseline that outputs the input echo's RIR that is closest to the query Q in terms of the receiver pose r.

Table 1: RIR prediction results. All methods here train a single model to handle all seen/unseen environment queries. See Table 2 for comparisons with NAF [35], which trains one model per seen environment. All metrics use base 10^{-2} and lower is better. Results are statistically significant between our model and the nearest baselines ($p \leq 0.05$).

	Seen environments				*Unseen environments*			
Model	STFT	RTE	DRRE	MOSE	STFT	RTE	DRRE	MOSE
Nearest Neighbor	4.65	1.15	385	24.4	4.87	1.26	391	28.0
Linear Interpolation	4.44	1.22	393	24.3	4.67	1.32	403	27.2
AnalyticalRIR++	2.94	0.98	463	28.1	3.02	1.19	467	29.4
Fast-RIR [53]++	1.37	1.25	137	13.7	1.45	1.61	369	15.2
FEW-SHOTRIR (Ours)	**1.10**	**0.43**	**106**	**8.66**	**1.22**	**0.65**	**164**	**10.5**
Ours w/ $N = 1$	1.69	0.74	362	17.2	1.70	0.90	372	17.4
Ours w/o echoes	1.63	0.63	334	19.5	1.67	0.95	357	20.0
Ours w/o vision	1.63	0.67	332	19.2	1.58	0.83	347	19.3
Ours w/o L_D	1.39	1.60	347	14.0	1.44	2.11	363	14.5

- **Linear Interpolation:** a naive baseline that computes the top four closest observation poses for the query receiver, and outputs the linear interpolation of the corresponding echoes' RIRs.
- **AnalyticalRIR++:** We modify our model to predict RT60 and DRR for the query using the egocentric observations. The modification uses the same transformer encoder-decoder pair, but replaces the transposed convolutions with fully-connected layers for RT60 or DRR prediction. It then *analytically* shapes an exponentially decaying white noise [33] on the basis of these two parameters to estimate the target RIR.
- **Fast-RIR [53]++:** Fast-RIR [53] is a state-of-the-art model that trains a GAN [23] to synthesize RIRs for rectangular rooms on the basis of environment and acoustic attributes, like scene size and RT60, which it assumes to be known a priori. Since FEW-SHOTRIR makes no such assumptions and is not restricted to rectangular rooms, we improve this method into Fast-RIR++: we use our modified model for AnalyticalRIR++ to estimate both the target RT60 and DRR, and use panoramic depth images at the query source and receiver to infer the scene size. We also train this model by augmenting the originally proposed objective with our L_D loss to further improve its performance.
- **Neural Acoustic Fields (NAF) [35]:** a state-of-the-art model that uses an implicit scene representation [41] to model RIRs. As discussed above, a NAF model can only predict new RIRs in the same training scene; it cannot generalize to an unseen environment without retraining a new model from scratch to fit the new scene.

Evaluation Metrics. We consider four metrics: 1) **STFT** Error, which measures the average error between predicted and target RIRs at the spectrogram level; 2) **RT60 Error (RTE)** [59, 52, 53], which measures the error in the RT60 value for our predicted RIRs. 3) **DRR Error (DRRE)** [52], which measures the error in the estimated energy ratio between direct and reverberant sounds in an RIR; and 4) **Mean Opinion Score Error (MOSE)** [9], which uses a deep learning objective [34] to measure the difference in perceptual quality between a prediction and the target when convolved with human speech. While STFT Error measures the fine-grained agreement of a prediction to the target, RTE and DRRE capture the extent of acoustic mismatch in a prediction, and MOSE evaluates the level of perceptual realism for human speech.

5.1 RIR Prediction Results

Table 1 (top) reports our main results. The naive Nearest Neighbor and Linear Interpolation baselines incur very high STFT error, which shows that using echoes from poses that are spatially close to the query receiver as proxy predictions are insufficient, emphasizing the difficulty of the task. AnalyticalRIR++ fares better than the naive baselines on STFT and RTE but has a higher DRRE and MOSE, showing that reconstructing an RIR using simple waveform statistics is not enough. Fast-RIR++ shows the strongest performance among the baselines. Its improvement over AnalyticalRIR++, with which it shares the RT60 and DRR predictors, shows that high-quality RIR prediction benefits from learned methods that go beyond estimating simple acoustic parameters.

Table 2: RIR prediction results for our model vs. NAF [35]. All metrics use base 10^{-2}.

	Seen environments (3)								*Unseen environments (all)*			
	Seen zones				*Unseen zones*							
Model	STFT	RTE	DRRE	MOSE	STFT	RTE	DRRE	MOSE	STFT	RTE	DRRE	MOSE
NAF	2.31	10.2	523	36.1	2.22	2.65	322	34.7	3.62	5.11	463	56.6
Ours	**0.90**	**1.97**	**95.7**	**7.08**	**1.58**	**1.25**	**155**	**13.6**	**1.22**	**0.65**	**164**	**10.5**

Model	STFT	RTE	DRR	MOSE
Nearest Neighbor	6.88	68.8	386	22.7
Linear Interpolation	6.61	68.7	388	21.5
AnalyticalRIR++	3.37	7.95	474	26.0
NAF [35]	3.62	51.1	367	56.6
Fast-RIR [53]++	1.58	**1.23**	436	17.1
FEW-SHOTRIR (Ours)	**1.51**	1.30	**202**	**14.0**

Table 3: RIR prediction results with ambient environment sounds in *unseen* environments. All metrics use base 10^{-2}.

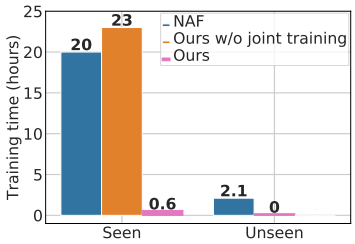


Figure 3: Training time comparison vs. NAF [35]

Our model outperforms all baselines by a statically significant margin ($p \leq 0.05$) on both *seen* and *unseen* environments. This shows that our approach facilitates environment acoustics modeling in a way that generalizes to novel environments without any retraining. Furthermore, its performance improvement over Fast-RIR [53]++ emphasizes the advantage of directly predicting RIRs on the basis of the implicit acoustic model inferred from egocentric observations, as opposed to indirect synthesis of RIRs by first estimating high-level acoustic characteristics for the target. As expected, our model has more limited success for very far-field queries; widely separated source and receivers make modeling late reverb difficult (see Supp for details).

FEW-SHOTRIR (Ours) vs. NAF [35]. Recall that, unlike our approach, NAF requires training one model per environment. Thus, for fair comparison, we train one model per scene for both NAF and our method. Due to the high computational cost of training NAF (as we discuss later) we limit our training to three large *seen* environments. Further, we split each seen environment into *seen zones*, which we use for training and also testing the models' interpolation capabilities, and *unseen zones*, which test intra-scene generalization. To give NAF access to our model's observations, we finetune it on our model's echo inputs before testing. For *unseen* environments, our model adopts the setup from the previous section, whereas we train NAF from scratch on our model's observed echoes; note that NAF's scene-specificity does not allow finetuning of a model trained on a seen environment.

Table 2 shows the results. Our model significantly ($p \leq 0.05$) outperforms NAF [35] on seen environments when considering both *seen* and *unseen zones*. The *seen zone* results underscore the better interpolation capabilities of our model in comparison to NAF when tested on held-out queries from the training zones. Our method's improvement over NAF on *unseen zones* shows that our model design and training objective lead to much better intra-scene generalization, even when NAF is separately finetuned on the observation sets from the *unseen zones*. While NAF improves over the naive baselines from Table 1 on STFT error, it does worse than other methods on most metrics. This demonstrates that just learning to predict a limited amount of echoes contained in the observation set of our model is insufficient to accurately model acoustics for unseen environments.

Figure 3 compares the training cost between NAF [35] and our model using wall clock time, when both models are trained on 8 NVIDIA Quadro RTX 6000 GPUs. When we train one model per environment, NAF takes 20 hours to converge on average, while our model takes 23 hours. However, our model design allows us to train one model jointly on all 56 Matterport3D training scenes in 32 hours, which reduces the average training time by $50\times$—down to 0.6 hours per environment. Moreover, for unseen environments, training NAF on echoes requires 2.1 hours for each observation set. In contrast, our model design enables training on a large number of scenes at a much lower average cost, while also allowing generalization to novel environments without further training.

Model	*Seen* SLE	DPE	*Unseen* SLE	DPE
True RIR (*Upper bound*)	14.9	0.97	17.0	1.25
Nearest Neighbor	202	1.50	214	1.57
Linear Interpolation	202	1.39	213	1.49
AnalyticalRIR++	254	1.64	270	1.69
NAF [35]	–	–	329	1.68
Fast-RIR [53]++	168	1.39	201	1.52
FEW-SHOTRIR (Ours)	**50.3**	**1.35**	**64.6**	**1.45**

Table 4: Downstream task evaluation of RIR predictions for sound source localization and depth estimation. All metrics use a base of 10^{-2} and lower is better.

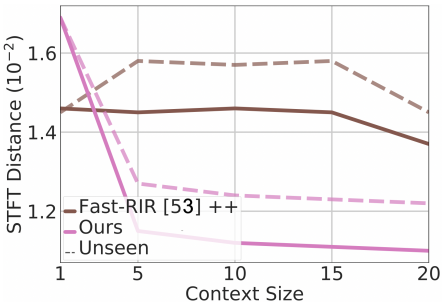


Figure 4: STFT error vs. context size N.

5.2 Model Analysis

Ablations. In Table 1 (bottom) we ablate the components of our model. When removing one of the modalities from the input, we see a drop in performance, which indicates that our model leverages the complementary information from both vision and audio to learn a better implicit model of the scene. We also observe a performance drop across all metrics, especially on the RTE metric, upon removing our energy decay matching loss L_D. This shows that having L_D as part of the training objective allows our model to better capture desirable reverberation characteristics for the target query, like RT60, while also additionally helping to score better on other metrics. Furthermore, we see that reducing the observation set to just 1 sample, i.e., $N = 1$, impacts our model's performance. However, even under this extreme condition, our model still shows better generalization compared to several baselines. We further investigate the impact of context size on our model's performance in Figure 4. Our model already reduces the error significantly using a context size of 5, with diminishing reductions as it gets a larger context. This plot also highlights the low-shot success of our model vs. the strongest baseline, Fast-RIR++.

Ambient environment sounds. We test our model's ability to generalize in the presence of ambient and background sounds. To that end, we repeat the experiment from Sec.5.1 where this time we insert a random ambient or background sound (e.g., running heater, dripping water). This background noise impacts the echoes input to our model. Table 3 reports the results. Even in this more challenging setting, our method substantially improves over all methods on almost all metrics.

Qualitative results. Figure 5 shows two RIR prediction scenarios for our model: *high reverberation*, where the query receiver is located close to the source in a very narrow and reverberant corridor surrounded by walls, and *low reverberation*, where the source and receiver are spread apart in a more open space. Our model shares the same observation samples across these settings. With high reverb, our model focuses on vision due to its ability to better reveal the compact geometry of the surroundings and its effects on scene acoustics, whereas echoes are distorted from strong reverberation. For low reverb, echoes are probably more informative about the acoustics of the more open surroundings due to their long-range nature. However, in both cases, our model prioritizes samples that provide good coverage of the overall scene, rather than just scoping out the local area around the query. This allows our model to make predictions that closely match the targets.

5.3 Downstream Applications for RIR Inference: Source Localization and Depth Estimation

Next, we consider two downstream tasks inspired by AR/VR and robotics: sound source localization and depth estimation from echoes. For both tasks, spatial audio generated by more accurate RIRs should translate into better representation of the true acoustics, and hence better downstream results.

We train a model for each task using ground truth RIR magnitude spectrograms and evaluate using the predicted magnitude spectrograms from our model and all baselines for the same set of queries from both *seen* and *unseen* environments. Table 4 reports the results. DPE is the average L_1 error between a normalized depth target and its prediction, and SLE is the average L_1 error in prediction

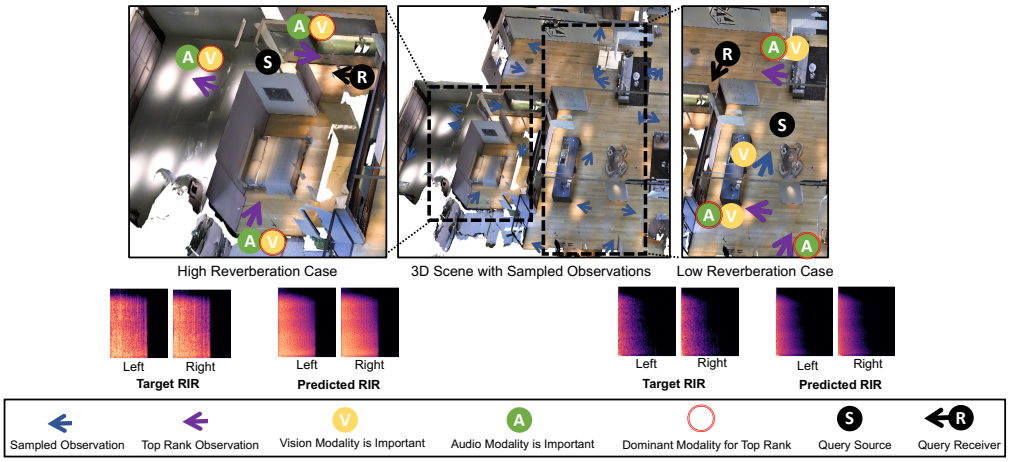


Figure 5: RIR predictions for a high and low reverberation case, where our model uses the same observations in both cases. For high reverb, our model relies more on vision than echoes for inferring scene acoustics, since echoes could be misleading in this case due to its long reverberation tail. For low reverb, our model uses echoes more, likely because their long-range nature better informs about the acoustics of the more open surroundings.

of the source location (in meters) relative to the receiver for a query. Our method outperforms all baselines by a statistically significant margin ($p \leq 0.05$). In particular, for the more difficult *unseen* environments, our model reduces the error relative to the ground truth upper bound by 74% for SLE and 25% for DPE when compared to Fast-RIR++, highlighting that our model's predictions capture spatial and directional cues more precisely than all other baselines and existing methods.

6 Potential Societal Impact

Our model enables modeling the acoustics in a 3D scene using only few observations. This has multiple applications with a positive impact. For example, accurate modeling of the scene acoustics enables a robot to locate a sounding object more efficiently (like finding a crying baby, or locating a broken vase). Additionally, this allows for a truly immersive experience for the user in augmented and virtual reality applications. However, RIR generative models allow the user to match the acoustic reverberation in their speech to an arbitrary scene type, and hence hide their true location from the receiver, which may have both positive and negative implications. Finally, our model uses visual samples from the environment for more accurate modeling of the acoustic properties of the scene. However, the dataset used in our experiments contains mainly indoor spaces that are of western designs, and with a certain object distribution that is common to such spaces. This may bias models trained on such data toward similar types of scenes and reduce generalization to scenes from other cultures. More innovations in the model design to handle strong shifts in scene layout and object distribtutions, as well as more diverse datasets are needed to mitigate the impact of such possible biases.

7 Conclusion

We introduced a model to infer arbitrary RIRs having observed only a small number of echoes and images in the space. Our approach helps tackle key challenges in modeling acoustics from limited observations, generalizing to unseen environments without retraining, and enforcing desired acoustic properties in the predicted RIRs. The results show its promise: substantial gains over existing models, faster training, and benefits for downstream source localization and depth estimation. In future work, we plan to explore ways to optimize the placement of the observation set and explore ways to curate large-scale real world data for sim2real transfer.

Acknowledgements: Thanks to Tushar Nagarajan and Kumar Ashutosh for feedback on paper drafts. UT Austin is supported in part by the IFML NSF AI Institute, NSF CCRI, and DARPA L2M. K.G. is paid as a research scientist by Meta, and C.C. was a visiting student researcher at Facebook AI Research when this work was done.

References

[1] Triantafyllos Afouras, Joon Son Chung, and Andrew Zisserman. The conversation: Deep audio-visual speech enhancement. *arXiv preprint arXiv:1804.04121*, 2018.

[2] Triantafyllos Afouras, Andrew Owens, Joon Son Chung, and Andrew Zisserman. Self-supervised learning of audio-visual objects from video. In *European Conference on Computer Vision*, pages 208–224. Springer, 2020.

[3] Jont Allen and David Berkley. Image method for efficiently simulating small-room acoustics. *The Journal of the Acoustical Society of America*, 65:943–950, 04 1979.

[4] Stefan Bilbao. Modeling of complex geometries and boundary conditions in finite difference/finite volume time domain room acoustics simulation. *Trans. Audio, Speech and Lang. Proc.*, 21(7):1524–1533, jul 2013.

[5] Chunxiao Cao, Zhong Ren, Carl Schissler, Dinesh Manocha, and Kun Zhou. Interactive sound propagation with bidirectional path tracing. *ACM Trans. Graph.*, 35(6), nov 2016.

[6] Chakravarty R. Alla Chaitanya, Nikunj Raghuvanshi, Keith W. Godin, Zechen Zhang, Derek Nowrouzezahrai, and John M. Snyder. Directional sources and listeners in interactive sound propagation using reciprocal wave field coding. *ACM Trans. Graph.*, 39(4), jul 2020.

[7] Angel Chang, Angela Dai, Thomas Funkhouser, Maciej Halber, Matthias Niessner, Manolis Savva, Shuran Song, Andy Zeng, and Yinda Zhang. Matterport3d: Learning from rgb-d data in indoor environments. *arXiv preprint arXiv:1709.06158*, 2017. Matterport3D license available at http://kaldir.vc.in.tum.de/matterport/MP_TOS.pdf.

[8] Changan Chen, Ziad Al-Halah, and Kristen Grauman. Semantic audio-visual navigation. *CoRR*, abs/2012.11583, 2020.

[9] Changan Chen, Ruohan Gao, Paul Calamia, and Kristen Grauman. Visual acoustic matching. *arXiv preprint arXiv:2202.06875*, 2022.

[10] Changan Chen, Unnat Jain, Carl Schissler, Sebastia Vicenc Amengual Gari, Ziad Al-Halah, Vamsi Krishna Ithapu, Philip Robinson, and Kristen Grauman. Soundspaces: Audio-visual navigation in 3d environments. In *European Conference on Computer Vision*, pages 17–36. Springer, 2020.

[11] Changan Chen, Sagnik Majumder, Ziad Al-Halah, Ruohan Gao, Santhosh Kumar Ramakrishnan, and Kristen Grauman. Audio-visual waypoints for navigation. *CoRR*, abs/2008.09622, 2020.

[12] Changan Chen, Wei Sun, David Harwath, and Kristen Grauman. Learning audio-visual dereverberation. *arXiv preprint arXiv:2106.07732*, 2021.

[13] Jesper Haahr Christensen, Sascha Hornauer, and X Yu Stella. Batvision: Learning to see 3d spatial layout with two ears. In *2020 IEEE International Conference on Robotics and Automation (ICRA)*, pages 1581–1587. IEEE, 2020.

[14] Victoria Dean, Shubham Tulsiani, and Abhinav Gupta. See, hear, explore: Curiosity via audio-visual association. In H. Larochelle, M. Ranzato, R. Hadsell, M.F. Balcan, and H. Lin, editors, *Advances in Neural Information Processing Systems*, volume 33, pages 14961–14972. Curran Associates, Inc., 2020.

[15] James Eaton, Nikolay D. Gaubitch, Alastair H. Moore, and Patrick A. Naylor. Estimation of room acoustic parameters: The ace challenge. *IEEE/ACM Transactions on Audio, Speech, and Language Processing*, 24(10):1681–1693, 2016.

[16] Ariel Ephrat, Inbar Mosseri, Oran Lang, Tali Dekel, Kevin Wilson, Avinatan Hassidim, William T Freeman, and Michael Rubinstein. Looking to listen at the cocktail party: A speaker-independent audio-visual model for speech separation. *arXiv preprint arXiv:1804.03619*, 2018.

[17] Angelo Farina. Simultaneous measurement of impulse response and distortion with a swept-sine technique. *Journal of the Audio Engineering Society*, February 2000.

[18] Thomas Funkhouser, Nicolas Tsingos, Ingrid Carlbom, Gary Elko, Mohan Sondhi, James E. West, Gopal Pingali, Patrick Min, and Addy Ngan. A beam tracing method for interactive architectural acoustics, 2003.

[19] Hannes Gamper and Ivan J. Tashev. Blind reverberation time estimation using a convolutional neural network. In *2018 16th International Workshop on Acoustic Signal Enhancement (IWAENC)*, pages 136–140, 2018.

[20] Chuang Gan, Yiwei Zhang, Jiajun Wu, Boqing Gong, and Joshua B Tenenbaum. Look, listen, and act: Towards audio-visual embodied navigation. In *2020 IEEE International Conference on Robotics and Automation (ICRA)*, pages 9701–9707. IEEE, 2020.

[21] Ruohan Gao, Changan Chen, Ziad Al-Halab, Carl Schissler, and Kristen Grauman. Visualechoes: Spatial image representation learning through echolocation. In *ECCV*, 2020.

[22] Ruohan Gao and Kristen Grauman. 2.5 d visual sound. In *Proceedings of the IEEE/CVF Conference on Computer Vision and Pattern Recognition*, pages 324–333, 2019.

[23] Ian Goodfellow, Jean Pouget-Abadie, Mehdi Mirza, Bing Xu, David Warde-Farley, Sherjil Ozair, Aaron Courville, and Yoshua Bengio. Generative adversarial nets. In Z. Ghahramani, M. Welling, C. Cortes, N. Lawrence, and K.Q. Weinberger, editors, *Advances in Neural Information Processing Systems*, volume 27. Curran Associates, Inc., 2014.

[24] Kaiming He, Xiangyu Zhang, Shaoqing Ren, and Jian Sun. Deep residual learning for image recognition. In *Proceedings of the IEEE conference on computer vision and pattern recognition*, pages 770–778, 2016.

[25] Martin Holters, Tobias Corbach, and Udo Zölzer. Impulse response measurement techniques and their applicability in the real world, 2009.

[26] Jen-Cheng Hou, Syu-Siang Wang, Ying-Hui Lai, Yu Tsao, Hsiu-Wen Chang, and Hsin-Min Wang. Audio-visual speech enhancement using multimodal deep convolutional neural networks. *IEEE Transactions on Emerging Topics in Computational Intelligence*, 2(2):117–128, 2018.

[27] Di Hu, Rui Qian, Minyue Jiang, Xiao Tan, Shilei Wen, Errui Ding, Weiyao Lin, and Dejing Dou. Discriminative sounding objects localization via self-supervised audiovisual matching. *Advances in Neural Information Processing Systems*, 33:10077–10087, 2020.

[28] Sergey Ioffe and Christian Szegedy. Batch normalization: Accelerating deep network training by reducing internal covariate shift. In Francis Bach and David Blei, editors, *Proceedings of the 32nd International Conference on Machine Learning*, volume 37 of *Proceedings of Machine Learning Research*, pages 448–456, Lille, France, 07–09 Jul 2015. PMLR.

[29] Hao Jiang, Calvin Murdock, and Vamsi Krishna Ithapu. Egocentric deep multi-channel audio-visual active speaker localization. *arXiv preprint arXiv:2201.01928*, 2022.

[30] Diederik P Kingma and Jimmy Ba. Adam: A method for stochastic optimization. *arXiv preprint arXiv:1412.6980*, 2014.

[31] Florian Klein, Annika Neidhardt, and Marius Seipel. Real-time estimation of reverberation time for selection of suitable binaural room impulse responses. *Audio for Virtual, Augmented and Mixed Realities: Proceedings of ICSA 2019; 5th International Conference on Spatial Audio; September 26th to 28th, 2019, Ilmenau, Germany*, page 145–150, Nov 2019.

[32] Homare Kon and Hideki Koike. Estimation of late reverberation characteristics from a single two-dimensional environmental image using convolutional neural networks. *Journal of the Audio Engineering Society*, 67(7/8):540–548, July 2019.

[33] K Lebart, J.-M Boucher, and P Denbigh. A new method based on spectral subtraction for speech dereverberation. *Acta Acustica united with Acustica*, 87:359–366, 05 2001.

[34] Chen-Chou Lo, Szu-Wei Fu, Wen-Chin Huang, Xin Wang, Junichi Yamagishi, Yu Tsao, and Hsin-Min Wang. Mosnet: Deep learning based objective assessment for voice conversion. In *Proc. Interspeech 2019*, 2019.

[35] Andrew Luo, Yilun Du, Michael J Tarr, Joshua B Tenenbaum, Antonio Torralba, and Chuang Gan. Learning neural acoustic fields. *arXiv preprint arXiv:2204.00628*, 2022.

[36] Wolfgang Mack, Shuwen Deng, and Emanuël A. P. Habets. Single-channel blind direct-to-reverberation ratio estimation using masking. In Helen Meng, Bo Xu, and Thomas Fang Zheng, editors, *Interspeech 2020, 21st Annual Conference of the International Speech Communication Association, Virtual Event, Shanghai, China, 25-29 October 2020*, pages 5066–5070. ISCA, 2020.

[37] Sagnik Majumder, Ziad Al-Halah, and Kristen Grauman. Move2hear: Active audio-visual source separation. In *Proceedings of the IEEE/CVF International Conference on Computer Vision*, pages 275–285, 2021.

[38] Sagnik Majumder, Ziad Al-Halah, and Kristen Grauman. Active audio-visual separation of dynamic sound sources. *arXiv preprint arXiv:2202.00850*, 2022.

[39] Ravish Mehra, Lakulish Antani, Sujeong Kim, and Dinesh Manocha. Source and listener directivity for interactive wave-based sound propagation. *IEEE Transactions on Visualization and Computer Graphics*, 20(4):495–503, apr 2014.

[40] Daniel Michelsanti, Zheng-Hua Tan, Shi-Xiong Zhang, Yong Xu, Meng Yu, Dong Yu, and Jesper Jensen. An overview of deep-learning-based audio-visual speech enhancement and separation. *IEEE/ACM Transactions on Audio, Speech, and Language Processing*, 2021.

[41] Ben Mildenhall, Pratul P Srinivasan, Matthew Tancik, Jonathan T Barron, Ravi Ramamoorthi, and Ren Ng. Nerf: Representing scenes as neural radiance fields for view synthesis. In *European conference on computer vision*, pages 405–421. Springer, 2020.

[42] Damian Murphy, Antti Kelloniemi, Jack Mullen, and Simon Shelley. Acoustic modeling using the digital waveguide mesh. *IEEE Signal Processing Magazine*, 24(2):55–66, 2007.

[43] Vinod Nair and Geoffrey E. Hinton. Rectified linear units improve restricted boltzmann machines. In *ICML*, pages 807–814, 2010.

[44] Andrew Owens and Alexei A Efros. Audio-visual scene analysis with self-supervised multisensory features. In *Proceedings of the European Conference on Computer Vision (ECCV)*, pages 631–648, 2018.

[45] Vassil Panayotov, Guoguo Chen, Daniel Povey, and Sanjeev Khudanpur. Librispeech: An asr corpus based on public domain audio books. In *2015 IEEE International Conference on Acoustics, Speech and Signal Processing (ICASSP)*, pages 5206–5210, 2015.

[46] Karol J. Piczak. ESC: Dataset for Environmental Sound Classification. In *Proceedings of the 23rd Annual ACM Conference on Multimedia*, pages 1015–1018. ACM Press, 2015.

[47] Senthil Purushwalkam, Sebastia Vicenc Amengual Gari, Vamsi Krishna Ithapu, Carl Schissler, Philip Robinson, Abhinav Gupta, and Kristen Grauman. Audio-visual floorplan reconstruction. In *Proceedings of the IEEE/CVF International Conference on Computer Vision*, pages 1183–1192, 2021.

[48] Kranthi Kumar Rachavarapu, Aakanksha, Vignesh Sundaresha, and A. N. Rajagopalan. Localize to binauralize: Audio spatialization from visual sound source localization. In *Proceedings of the IEEE/CVF International Conference on Computer Vision (ICCV)*, pages 1930–1939, October 2021.

[49] Nikunj Raghuvanshi and John Snyder. Parametric wave field coding for precomputed sound propagation. *ACM Trans. Graph.*, 33(4), jul 2014.

[50] Nikunj Raghuvanshi and John Snyder. Parametric directional coding for precomputed sound propagation. *ACM Trans. Graph.*, 37(4), jul 2018.

[51] Anton Ratnarajah, Zhenyu Tang, and Dinesh Manocha. Ir-gan: Room impulse response generator for far-field speech recognition. *arXiv preprint arXiv:2010.13219*, 2020.

[52] Anton Ratnarajah, Zhenyu Tang, and Dinesh Manocha. Ts-rir: Translated synthetic room impulse responses for speech augmentation. *arXiv preprint arXiv:2103.16804*, 2021.

[53] Anton Ratnarajah, Shi-Xiong Zhang, Meng Yu, Zhenyu Tang, Dinesh Manocha, and Dong Yu. Fast-rir: Fast neural diffuse room impulse response generator. In *ICASSP 2022-2022 IEEE International Conference on Acoustics, Speech and Signal Processing (ICASSP)*, pages 571–575. IEEE, 2022.

[54] Luca Remaggi, Hansung Kim, Philip J. B. Jackson, and Adrian Hilton. Reproducing real world acoustics in virtual reality using spherical cameras. *Journal of the Audio Engineering Society*, March 2019.

[55] Olaf Ronneberger, Philipp Fischer, and Thomas Brox. U-net: Convolutional networks for biomedical image segmentation. In *International Conference on Medical image computing and computer-assisted intervention*, pages 234–241. Springer, 2015.

[56] Mostafa Sadeghi, Simon Leglaive, Xavier Alameda-Pineda, Laurent Girin, and Radu Horaud. Audio-visual speech enhancement using conditional variational auto-encoders. *IEEE/ACM Transactions on Audio, Speech, and Language Processing*, 28:1788–1800, 2020.

[57] Lauri Savioja and U. Peter Svensson. Overview of geometrical room acoustic modeling techniques. *The Journal of the Acoustical Society of America*, 138 2:708–30, 2015.

[58] Manolis Savva, Abhishek Kadian, Oleksandr Maksymets, Yili Zhao, Erik Wijmans, Bhavana Jain, Julian Straub, Jia Liu, Vladlen Koltun, Jitendra Malik, Devi Parikh, and Dhruv Batra. Habitat: A Platform for Embodied AI Research. In *Proceedings of the IEEE/CVF International Conference on Computer Vision (ICCV)*, 2019.

[59] Nikhil Singh, Jeff Mentch, Jerry Ng, Matthew Beveridge, and Iddo Drori. Image2reverb: Cross-modal reverb impulse response synthesis. In *Proceedings of the IEEE/CVF International Conference on Computer Vision*, pages 286–295, 2021.

[60] Vincent Sitzmann, Julien Martel, Alexander Bergman, David Lindell, and Gordon Wetzstein. Implicit neural representations with periodic activation functions. *Advances in Neural Information Processing Systems*, 33:7462–7473, 2020.

[61] Nitish Srivastava, Geoffrey Hinton, Alex Krizhevsky, Ilya Sutskever, and Ruslan Salakhutdinov. Dropout: A simple way to prevent neural networks from overfitting. *Journal of Machine Learning Research*, 15(56):1929–1958, 2014.

[62] Guy-Bart Stan, Jean-Jacques Embrechts, and Dominique Archambeau. Comparison of different impulse response measurement techniques. *Journal of the Audio Engineering Society*, 50(4):249–262, April 2002.

[63] Yi Sun, Xiaogang Wang, and Xiaoou Tang. Deeply learned face representations are sparse, selective, and robust. In *Proceedings of the IEEE conference on computer vision and pattern recognition*, pages 2892–2900, 2015.

[64] Vesa Välimäki, Julian D. Parker, Lauri Savioja, Julius O. Smith, and Jonathan S. Abel. More than 50 years of artificial reverberation. In Stefan Goetze and Ann Spriet, editors, *Proc. 60th International Conference of the Audio Engineering Society*, United States, 2016. Audio Engineering Society. AES International Conference on Dereverberation and Reverberation of Audio, Music, and Speech, DREAMS ; Conference date: 03-02-2016 Through 05-02-2016.

[65] Ashish Vaswani, Noam Shazeer, Niki Parmar, Jakob Uszkoreit, Llion Jones, Aidan N Gomez, Łukasz Kaiser, and Illia Polosukhin. Attention is all you need. *Advances in neural information processing systems*, 30, 2017.

[66] Stephan Werner, Florian Klein, Annika Neidhardt, Ulrike Sloma, Christian Schneiderwind, and Karlheinz Brandenburg. Creation of auditory augmented reality using a position-dynamic binaural synthesis system—technical components, psychoacoustic needs, and perceptual evaluation. *Applied Sciences*, 11(3), 2021.

[67] Feifei Xiong, Stefan Goetze, Birger Kollmeier, and Bernd T. Meyer. Joint estimation of reverberation time and early-to-late reverberation ratio from single-channel speech signals. *IEEE/ACM Transactions on Audio, Speech, and Language Processing*, 27(2):255–267, 2019.

[68] Xudong Xu, Hang Zhou, Ziwei Liu, Bo Dai, Xiaogang Wang, and Dahua Lin. Visually informed binaural audio generation without binaural audios. In *Proceedings of the IEEE/CVF Conference on Computer Vision and Pattern Recognition (CVPR)*, pages 15485–15494, June 2021.

[69] Hang Zhao, Chuang Gan, Wei-Chiu Ma, and Antonio Torralba. The sound of motions. In *Proceedings of the IEEE/CVF International Conference on Computer Vision*, pages 1735–1744, 2019.

[70] Hang Zhou, Ziwei Liu, Xudong Xu, Ping Luo, and Xiaogang Wang. Vision-infused deep audio inpainting. In *Proceedings of the IEEE/CVF International Conference on Computer Vision*, pages 283–292, 2019.

[71] Hang Zhou, Xudong Xu, Dahua Lin, Xiaogang Wang, and Ziwei Liu. Sep-stereo: Visually guided stereophonic audio generation by associating source separation. *CoRR*, abs/2007.09902, 2020.

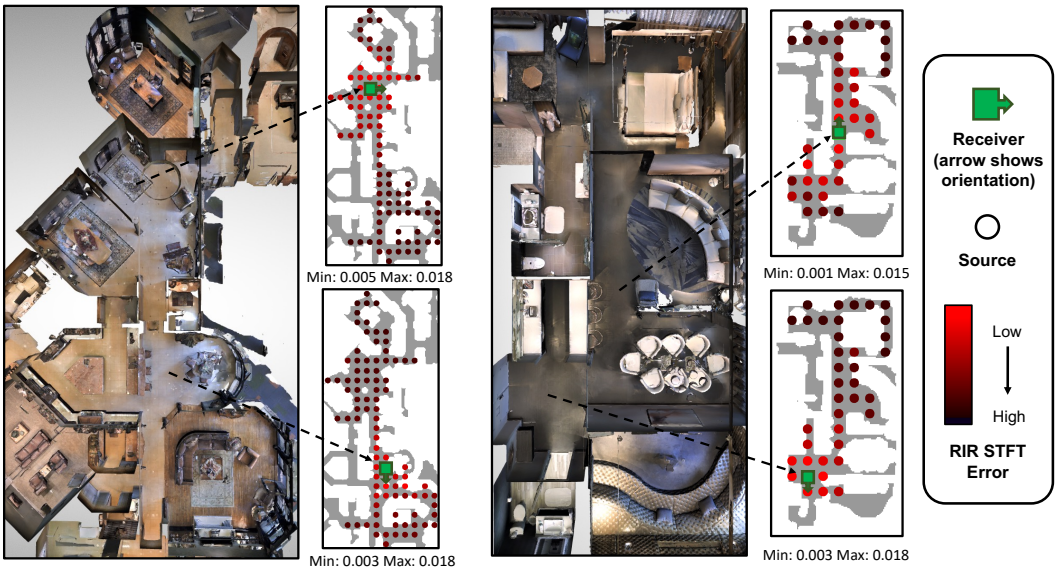


Figure 6: RIR prediction STFT error as a function of varying source locations (filled circles) for a given receiver (a green square with an arrow). We show two scenes and two examples per scene. The color of the circle at the source location indicates the STFT error in the RIR prediction associated with that source and receiver pair. The error in each example is normalized between the min and max values shown underneath the map.

8 Supplementary Material

In this supplementary material we provide additional details about:

- Video (with audio) for qualitative illustration of our task and qualitative evaluation of our model predictions (Sec. 8.1).
- Evaluation of the impact of the query source location on our model's prediction quality for a fixed receiver (Sec. 8.2).
- Audio dataset details (Sec. 8.3), as mentioned in Sec. 5 of the main paper.
- Model architecture details for RIR prediction (Sec. 8.4.1) and downstream tasks (Sec. 8.4.2), as noted in Sec. 5 of the main paper.
- Training hyperparameters (Sec. 8.5), as referenced in Sec. 5 of the main paper.

8.1 Supplementary Video

The supplementary video shows the perceptually realistic SoundSpaces [10] audio simulation platform that we use for our experiments, and provides a qualitative illustration of our task, Few-Shot Audio-Visual Learning of Environment Acoustics. Moreover, we qualitatively demonstrate our model's prediction quality by comparing the predictions with the ground truths, both at the RIR level and in terms of perceptual similarity when the RIRs are convolved with real-world monaural sounds, like speech and music. We also analyze common failure cases for our model (Sec. 5.1 in main) and qualitatively show how our model predictions can be used to successfully localize an audio source in a 3D environment. Please use headphones to hear the spatial audio correctly. The video is available at `http://vision.cs.utexas.edu/projects/fs_rir`.

8.2 Impact of the Source Location on the Prediction Error

In Fig. 6, we show the RIR prediction error as a function of different source locations for a fixed receiver location. As we can see, the prediction error tends to be small when the source is relatively close to the receiver, or there are no major obstacles along the path connecting them. This indicates that the model leverages the local geometry of the scene and the acoustic information captured from echoes for better predictions. However, the error increases when there are large distances between the source and receiver (Sec. 5.1 in main), and especially when there are major obstacles for audio propagation in between (e.g., walls, narrow corridors). Modeling how audio gets transformed on such a long path becomes very challenging due to the limited observations available to the model and the larger scene area that contributes to transforming the audio.

8.3 Audio Dataset

For computing the mean opinion score error (MOSE) [9] (Sec. 5 in main), we sample 5 second long speech clips from the LibriSpeech [45] dataset, which comprise both male and female speakers. For every test query, we randomly choose one of the sampled clips and convolve with the true RIR or a model's prediction for that query to estimate the corresponding mean opinion score (MOS) [34] and, subsequently, the error in MOS for a model's prediction relative to the true RIR. We use a 5-second-long temporal window for all model predictions and true RIRs when estimating their MOS.

For our experiment with ambient environment sounds (Sec. 5.2 in main), we use ambient sounds from the ESC-50 [46] dataset (e.g., dog barking, running water). For every test query, we randomly sample a location in the 3D scene for an ambient sound and play a randomly chosen 1 second long clip from the ESC-50 dataset at that location. To retrieve the observed binaural echo response A_i (Sec. 3 and 4.1 in main) in this setting, we first convolve the clean echo RIR for each observation O_i with the sinusoidal sweep sound, then mix it with the binaural the ambient sound for its pose P_i, and finally deconvolve using the inverse sweep (Sec. 4.1 in main).

We will publish the link to our datasets on our project page.

8.4 Architecture and Training

Here, we provide our architecture and additional training details for reproducibility. We will publish the link to our codebase on our project page.

8.4.1 Model Architectures for RIR Prediction

Visual Encoder. Our visual encoder f^V is a ResNet-18 [24] model (Sec. 4.1 in main) that takes egocentric RGB and depth images from the observation set, which are concatenated channel-wise, as input and produces a 512-dimensional feature.

Acoustic Encoder. Our acoustic encoder f^A is another ResNet-18 [24] (Sec. 4.1 in main) that separately encodes the binaural log magnitude spectrogram for an echo RIR A_i into a 512-dimensional feature.

Pose Encoder. To embed an observation pose P_i or a query source-receiver pair Q (Sec. 3 in main), we use sinusoidal positional encodings [65] (Sec. 4.1 in main) with 8 frequencies, which generate a 16-dimensional feature vector (the positional encodings comprise both sine and cosine components with 8 features per component) for every attribute of an observation pose or a query (i.e., x, y, and θ).

Modality Encoder. For our modality embedding m (Sec. 4.1 in main), we maintain a sparse lookup table of 8-dimensional learnable embeddings, which we index with 0 to retrieve the visual modality embedding (m_V) and 1 to retrieve the acoustic modality embedding (m_A).

Fusion Layer. To generate the multimodal memory S (Sec. 4.1 in main) for our context encoder (Sec. 4.1 in main), we separately concatenate the modality features (produced by f^V for vision and f^A for echo responses) for an observation, the corresponding sinusoidal pose embedding, and the modality embedding (m_V for visual features and m_A for acoustic features), and project using a single linear layer to 1024-dimensional embedding space. Similarly, to generate the query encoding q for our conditional RIR predictor (Sec. 4.2 in main), we use another linear layer to project the query's sinusoidal positional encodings to a 1024-dimensional feature vector. Furthermore, we don't use bias in any fusion layer.

Context Encoder. Our context encoder (Sec. 4.1 in main) is a transformer encoder [65] with 6 layers, 8 attention heads, a hidden size of 2048 and ReLU [63, 43] activations. Additionally, we use a dropout [61] of 0.1 in our context encoder.

Conditional RIR Predictor. Our conditional RIR predictor (Sec. 4.2 in main) has 2 components: 1) a transformer decoder [65] to perform cross-attention on the implicit representation C (Sec. 4.1 in main), which is produced by the previously described context encoder, using the query encoding q (Sec. 4.2 in main), and 2) a multi-layer transpose convolution network U (Sec. 4.2 in main) to upsample the decoder output d^Q and predict the magnitude spectrogram for the query Q in log space.

The transformer decoder [65] has the same architecture as our context encoder.

The transpose convolution network U comprises 7 layers in total. The first 6 layers are transpose convolutions with a kernel size of 4, stride of 2, input padding of 1, ReLU [63, 43] activations and BatchNorm [28]. The number of input channels for the transpose convolutions are 128, 512, 256, 128, 64 and 32, respectively. The last layer of U is a convolution layer with a kernel size of 3, stride of 1, padding of 1 along the height dimension and 2 along the width dimension, and 16 input channels. Finally, we switch off bias in all layers of U.

8.4.2 Model Architectures for Downstream Tasks

Sound Source Localization. We use a ResNet-18 [24] feature encoder that takes the log magnitude spectrogram of an RIR (predicted or ground truth as input). We take the encoded features and feed them to a single linear layer that predicts the location coordinates of a query's source relative to the query's receiver pose.

Depth Estimation. Following VisualEchoes [21], we use a U-net [55] that takes the log magnitude spectrogram of an echo as input and predicts the depth map (Sec. 5.3 in main) as seen from the echo's pose. The encoder of our U-net has 6 layers. The first layer is a convolution with a kernel size of 3, stride of 2, padding of 1 along the height dimension, and 2 input channels. The remaining 5 layers are convolutions with a kernel size of 4, padding of 1 and stride of 2. These 5 layers have 64, 64, 128, 256 and 512 input channels, respectively. Each convolution is followed by a ReLU activation [63, 43] and a BatchNorm [28].

The decoder of the U-net has 5 transpose convolution layers. Each transpose convolution has a kernel size of 4, stride of 2 and input padding of 1. Except for the last layer that uses a sigmoid activation function to generate depth maps, which are normalized such that all pixels are in the range of $[0, 1]$, each transpose convolution has a ReLU activation [63, 43] and a BatchNorm [28]. The decoder layers have 512, 1024, 512, 256 and 128 channels, respectively. We use skip connections between the encoder and the decoder starting with their second layer. We switch off bias in both the encoder and decoder.

8.5 Training Hyperparameters

In addition to the training details specified in main (Sec. 4.3 in main), we use a batch size of 24 during training. Furthermore, for every entry of the batch, we query our model with 60 arbitrary source-receiver pairs for the same observation set, which effectively increases the batch size further and improves training speed. Other training hyperparameters specific to our Adam [30] optimizer include $\beta_1 = 0.9$, $\beta_2 = 0.999$ and $\epsilon = 10^{-5}$.